

Banner appropriate to article type will appear here in typeset article

# Experimental measurement of the vorticity-strain alignment around extreme energy transfer events

Benjamin Musci<sup>1</sup> †, Bérengère Dubrulle<sup>1</sup>, Jean LeBris<sup>1</sup>, Damien Geneste<sup>1</sup>, Pierre Braganca<sup>2</sup>, Jean-Marc Foucaut<sup>2</sup>, Christophe Cuvier<sup>2</sup>, and Adam Cheminet<sup>1</sup>

<sup>1</sup>Université Paris-Saclay, CEA, CNRS, SPEC, CEA Paris-Saclay, F-91191 Gif sur Yvette, France

<sup>2</sup>Univ. Lille, CNRS, ONERA, Arts et Metiers Institute of Technology, Centrale Lille, UMR 9014 - Laboratoire de Mécanique des Fluides de Lille (LMFL) - Kampé de Fériet, Lille, F-59000, France

(Received xx; revised xx; accepted xx)

This work experimentally explores the alignment of the vorticity vector and the strain-rate tensor eigenvectors at locations of extreme upscale and downscale energy transfer. We show that the turbulent von Karman flow displays vorticity-strain alignment behavior across a large range of Reynolds numbers, which are very similar to previous studies on homogeneous, isotropic turbulence. We observe that this behavior is amplified for the largest downscale energy transfer events, which tend to be associated with sheet-like geometries. These events are also shown to have characteristics previously associated with high flow field non-linearity and singularities. In contrast the largest upscale energy transfer events display much different structures which showcase a strong preference for vortex-compression. We then show further evidence to the argument that strain-self-amplification is the most salient feature in characterizing cascade direction. Finally, we identify possible invariant behavior for the largest energy transfer events, even at scales near the Kolmogorov scale.

**Key words:** Authors should not enter keywords on the manuscript, as these must be chosen by the author during the online submission process and will then be added during the typesetting process (see [Keyword PDF](#) for the full list). Other classifications will be added at the same time.

---

**MSC Codes** (*Optional*) Please enter your MSC Codes here

## 1. Introduction

In turbulence there is little question that an energy cascade exists, whereby energy injected at the largest scales of a flow is eventually dissipated to heat by viscosity. However, there is still much to debate as to how this cascade works - the relevant mechanisms and flow structures, the validity of the so called “Richardson” cascade, and the degree of time and

† Email address for correspondence: benjamin.musci@cea.fr

**Abstract must not spill onto p.2**

space locality in the cascade - are all open questions (Tsinober 2009; Vela-Martín & Jiménez 2021; Johnson & Wilczek 2024).

Perhaps motivated by Richardson’s “whirl” centric poetic verse, a large portion of previous works focus on probing the cascade primarily through the characterization of the vorticity vector,  $\boldsymbol{\omega}$ , and secondly via the strain-rate tensor,  $\mathbf{S}$ , which is simply the symmetric portion of the velocity-gradient tensor,  $\mathbf{A} = \nabla \mathbf{u} = \partial u_i / \partial x_j$ . Much of the literature has focused on the alignment and interaction of  $\boldsymbol{\omega}_i = \epsilon_{ijk} \partial u_k / \partial x_j$  and the eigenvectors of  $S_{ij} = \frac{1}{2}(\partial u_i / \partial x_j + \partial u_j / \partial x_i)$  (as in Figure 1a), as they are thought to be the primary cause of non-linearity in vorticity dynamics (Hamlington *et al.* 2008). As such, there has been an effort to link the energy cascade with the geometry of  $\mathbf{A}$ , particularly as it is implicitly assumed in many sub-grid-scale turbulence models that the velocity-gradient at resolved (large) scales can be used to determine energy transfer at the unresolved (small) scales (Smagorinsky 1963; Vela-Martín & Jiménez 2021). We point the reader to the excellent recent review by Johnson & Wilczek (2024) for a more nuanced discussion of the current research, but we will highlight some of the more pertinent works here.

The eigenvectors of  $\mathbf{S}$  define its principal axes, which are also the directions of extremal strain. They are defined as  $\mathbf{e}_1, \mathbf{e}_2, \mathbf{e}_3$ , where  $\mathbf{e}_1$  and  $\mathbf{e}_3$  are always the most extensive and compressive vectors, respectively. Conversely, for incompressible flows  $\mathbf{e}_2$  can either be extensive or compressive depending on the local flow. One of the most consistent, but perhaps counterintuitive, findings in this field has been that  $\boldsymbol{\omega}$  has a prevalence to align with  $\mathbf{e}_2$  (also shown to be predominately extensive), and not  $\mathbf{e}_1$ , which would result in the maximal amount of vortex-stretching (Betchov 1956; Ashurst *et al.* 1987; Tsinober & Kit 1992; Hamlington *et al.* 2008; Buaria *et al.* 2020). These same works have also reported the more slight preference for  $\boldsymbol{\omega}$  to orient itself perpendicular to the most compressive strain axes,  $\mathbf{e}_3$ . An illustration of this preferred alignment is shown in Figure 1a. The prevalence of these findings across theory, direct numerical simulations (DNS), experiments and a range of turbulent flows lend credence to the idea that these vortex alignment preferences may be considered a universal feature of turbulent flows.

Despite the predominance of  $\boldsymbol{\omega}$  alignment with  $\mathbf{e}_2$ , other works provide arguments as to why it is nevertheless the alignment of  $\boldsymbol{\omega}$  and  $\mathbf{e}_1$  that is the main driver of enstrophy generation and energy cascade (Hamlington *et al.* 2008; Buxton & Ganapathisubramani 2010; Buaria & Pumir 2021). Looking at the individual contributions of each strain-rate eigenvector to enstrophy-production, some found the contribution from  $\mathbf{e}_1$  to be slightly larger than that of  $\mathbf{e}_2$ , with a difference that increased with Reynolds number,  $Re$  (Jimenez *et al.* 1993; Buaria *et al.* 2019; Zhou & Frank 2021). Hamlington *et al.* (2008) and Buaria & Pumir (2021) showed that the  $\boldsymbol{\omega} - \mathbf{e}_1$  alignment was achieved after removing the local, self-induced, strain-rate, while Xu *et al.* (2011) showed that this alignment occurred at some characteristic lag time. Other authors use the joint probability distribution of the second and third velocity gradient invariants ( a “QR plot”) to demonstrate the prevalence of vortex stretching over vortex compression. Buxton & Ganapathisubramani (2010) combined both approaches and found the  $\boldsymbol{\omega} - \mathbf{S}$  alignment for each region of QR space. While the alignment behavior of  $\mathbf{e}_2$  stayed the same throughout, areas with  $R < 0$  displayed  $\boldsymbol{\omega} - \mathbf{e}_1$  alignment. Thereby they argued that the extensive  $\mathbf{e}_1$  alignment is more important for determining enstrophy-production or destruction, and that the universally flat distribution of  $\mathbf{e}_1$  alignment in other works is due to the summation of the different behaviors throughout QR space.

On the other hand, many other works propose that the alignment of  $\boldsymbol{\omega}$  and  $\mathbf{S}$  is over-emphasized and instead the self-amplification of strain-rate is most important (Vincent & Meneguzzi 1994; Tsinober 1998, 2009; Carbone & Bragg 2020; Johnson 2020, 2021; Vela-Martín & Jiménez 2021). For instance Vincent & Meneguzzi (1994) presented evidence

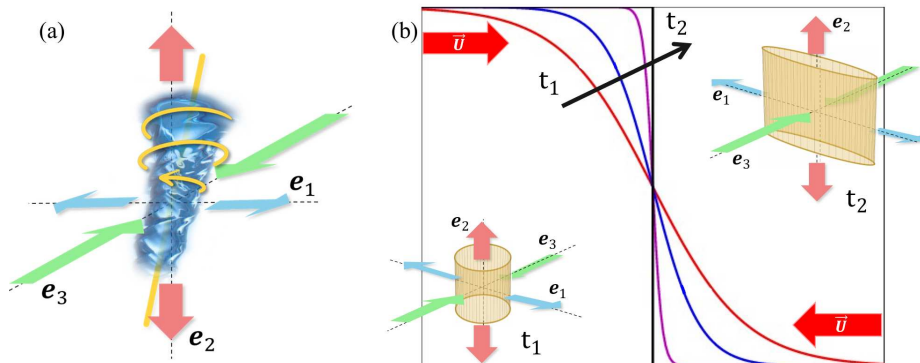


Figure 1: (a) Schematic of typical  $\omega - \mathbf{S}$  alignment.  $\omega$  is indicated by the yellow line and swirl. The baseline/universal preference for alignment between  $\omega - e_2$  is shown. To maximize vortex-stretching,  $\omega$  (yellow line) would be aligned more with  $e_1$ , which has been found generally to not be the case in turbulence. (b) Schematic illustrating strain-rate self-amplification (SSA) in a 1D and 3D sense. In 1D, an initial compressive strain (red line) causes the opposing velocities to steepen the negative gradient of the curves as time progresses, which in turn increases the compressive strain, until a singularity/shock forms (black line) as in the Burgers 1D equation. The same idea is illustrated in the 3D, where an initially cylindrical fluid parcel (or vortex) is compressed along one axis, and stretched in two others, in turn increasing the compressive strain.

that enstrophy-production is actually driven largely by the shear instability of vortex sheets. Similarly Tsinober (2009) showed the cascade is caused more via the compression of fluid elements and strain-self-amplification than by vortex stretching. A key to these arguments is the non-local nature of  $\omega - \mathbf{S}$  interactions, the direct relationship between strain and energy dissipation, and the highly non-linear nature of strain dominated regions (Tsinober 1998, 2009). Several related works used the QR space to claim that most nonlinear flow behavior occurs in areas with high strain-production, while nonlinearity is relatively repressed in regions of high vorticity (Tsinober 1998; Gulitski *et al.* 2007; Tsinober 2009). Further, while strain-production has been found to only depend on strain, vortex stretching has been shown to actually deplete strain-production (Betchov 1956; Tsinober 2009). Interestingly, Buaria *et al.* (2019) and Donzis *et al.* (2008) also found that while extreme strain events were co-located with equally large enstrophy events, intense vorticity events were accompanied by relatively less strain. The fact that enstrophy and strain share the same mean value, yet enstrophy appears more intermittent is thought to be due to the fact that vortex stretching amplifies vorticity while depleting strain (Buaria *et al.* 2019; Ishihara *et al.* 2009).

The behavior of the velocity-gradient during “extreme events” in the energy cascade is also of much interest. The link between  $\mathbf{A}$  morphology and extreme energy transfer events can be easily made by considering that in the 1D Burgers equation, strain-self-amplification is responsible for singularity and shock formation in the inviscid limit (Johnson & Wilczek 2024). This idea was extended to 3D with the so called “Restricted Euler” equation, which has been shown to produce finite time singularities in the absence of the anisotropic pressure Hessian and viscosity (Vieillefosse 1982, 1984). Notably, the morphologies which ought to bring about this singularity are those found ubiquitously in turbulent flows: two extensional strain directions ( $e_1, e_2$ ) and preferential  $\omega - e_2$  alignment, *i.e.* Figure 1a. Strain-self-amplification (illustrated in Figure 1b) occurs strictly due to the positivity of  $e_2$ , and it’s predicted that the singularity will occur along the region in QR space affiliated with that straining mechanism (Vieillefosse 1982, 1984; Johnson 2021; Johnson & Wilczek 2024). These ideas have been supported by other works investigating extreme events in enstrophy,

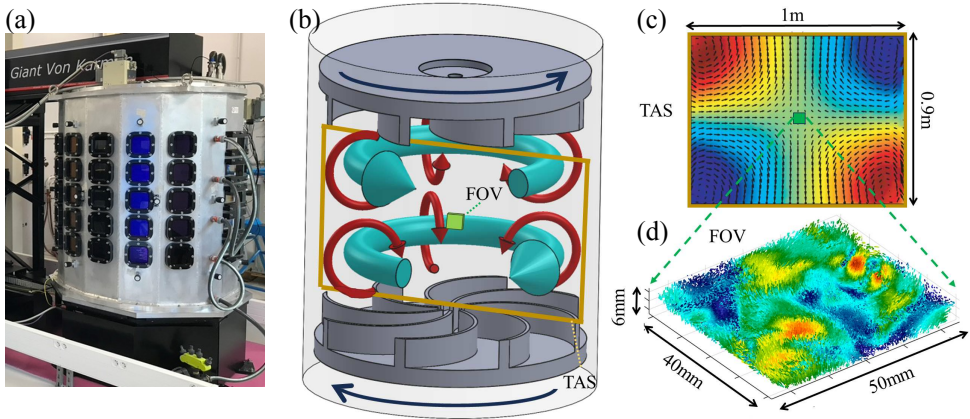


Figure 2: (a) Photo of the GvK experimental facility. (b) Schematic of the facility showing the direction of impeller rotation and time averaged flow. Two toruses revolve in the same direction as their nearest impeller, which induce counter rotating vortices that create the turbulent shear layer where the Field-of-View (FOV) is located. (c) Time averaged slice (TAS) shows the steady-state velocity field in the meridional plane and the relative size and position of the FOV (Cortet *et al.* 2010). The arrows show the velocity vectors in the axial-radial plane, while color maps to the azimuthal velocity from negative (blue) to positive (red). (d) One instant of the 80 000 particle trajectories found in the FOV. Color indicates velocity magnitude normalized by the impeller tip velocity (0 = blue, 1 = red).

which have simultaneously found enhanced  $\omega - e_2$  alignment, and a quasi-2D structure during the event (Jimenez *et al.* 1993; Buaria *et al.* 2019, 2020; Zhou & Frank 2021). Finally, Vela-Martín & Jiménez (2021) investigated the morphological and probabilistic differences between downscale and upscale energy transfers. They found these to be mainly driven by strain-dominated energy fluxes, where downscale transfer was most correlated with strain dominated regions. Additional investigation of the velocity-gradient structure for upscale energy transfer showed that while vortex stretching and compression exists in both cascade directions (albeit in different proportions), strain dominated regions depends strongly on cascade direction.

In this work we will combine approaches used in previous works to address several unanswered questions. Of main interest is how the morphology of the velocity-gradient behaves for the largest upscale and downscale energy transfer events. We will condition morphological statistics on energy transfer amplitude and make use of both the QR and  $\omega - \mathbf{S}$  alignment methods to probe the behavior. In the next sections we introduce our experimental facility (Section 2) and the main quantities of interest (Section 3), and then display non-conditioned morphological statistics (Section 4.1). We then provide the conditioned statistics in Section 4.2 and finish by discussing their implications from different perspectives in Section 5.

## 2. Experimental Giant von Karman Facility

The data presented in this work is purely experimental and is collected from the Giant von Kármán (GvK) facility at CEA Paris-Saclay. This state of the art facility has been described extensively in previous works, so we resort to a quick summary here (Dubrulle *et al.* 2022; Cheminet *et al.* 2021, 2022; Debue *et al.* 2021). The facility (Figure 2a) consists of a large cylindrical tank with radius ( $r$ ) and height (distance between impellers) of 0.5m and 0.9m, respectively - the radius to height aspect ratio is 1.8. The tank is filled with water that is

$Re$	$F$ [Hz]	$Re_\lambda$	$\langle \epsilon \rangle$ [ $\frac{m^2}{s^3}$ ]	$\eta$ [mm]	$\tau_\eta$ [ms]	$T_i$ [s]	$\frac{\tau_{acf}}{\tau_\eta}$	$F_a$ [Hz]	$\frac{\Delta x_p}{\eta}$	$N$
<b>6 269</b>	0.004	87	$1.89 \times 10^{-7}$	1.52	2 300	39.8	3.48	50	0.3	236
<b>39 180</b>	0.025	277	$4.63 \times 10^{-5}$	0.38	147	6.4	4.54	300	0.6	416
<b>156 719</b>	0.1	616	$2.96 \times 10^{-3}$	0.14	18	1.6	4.63	1 200	3.0	1 856

Table 1: Table of relevant experimental parameters for the three  $Re$  GvK data sets.

maintained at a constant temperature of  $20^\circ C$  by two cooling circuits located above and below the turbines, thus ensuring a statistically constant viscosity ( $\nu$ ) in the flow. The flow is driven to a turbulent steady-state via two counter-rotating impellers, which rotate at the same frequency ( $F$ ) and are used to change the integral scale Reynolds number ( $Re = 2\pi r^2 F/\nu$ ). The impellers have 8 curved blades (type TM87 as described in Ravelet *et al.* (2004)), and are rotated such that the concave portion of the blade advances through the fluid in a “scooping” direction.

The resulting flow is fully turbulent with a coherent, large-scale structure in the time-averaged sense (Figure 2b-c). This structure creates a homogenized and quasi-isotropic shear layer in the mid-plane of the cylinder, where the experimental measurements are carried out. The characteristic higher-order turbulent statistics in this area of the flow (*i.e.* Field of View, FOV, in Figure 2b-d) have been found to agree well with homogeneous isotropic turbulence (HIT) DNS results (Geneste *et al.* 2019; Debue *et al.* 2018a,b, 2021).

Time resolved 3D velocity fields are obtained using 4D Particle Tracking Velocimetry (PTV), whereby a high-speed laser (30 mJ pulse Nd:YLG) illuminates a volume ( $V = 50 \times 40 \times 6 \text{ mm}^3$ ) at the centered FOV, which is recorded using four cameras (Phantom Miro m340: 4.1 Megapixel CMOS sensors, with  $10 \mu\text{m}$  square pixels). The particles used are spherical polystyrene particles of  $5 \mu\text{m}$  diameter (Stokes number of  $S_{t,\tau_\eta} \leq 8.1 \times 10^{-5}$  for all cases). Particle tracks are obtained using the Davis10 “Shake-The-Box” algorithm (Schanz *et al.* 2016). In house codes are then used to go from Lagrangian particle trajectories to Eulerian velocity fields. This process has been validated and described previously by Cheminet *et al.* (2021). In short, a regularized B-spline filter is first applied on the Lagrangian trajectories to smooth out temporal noise on the tracks. Then a second regularized B-spline interpolation scheme (Gesemann *et al.* 2016) is used to project the velocity field onto a regular Eulerian grid.

The spatial resolution of our data is in turn determined by the number of particles in the FOV ( $N_p \approx 80,000$  on average) where the mean inter-particle distance is:  $\Delta x_p = (V/N_p)^{1/3}$ . When keeping constant flow and diagnostic parameters, increasing/decreasing the rotation frequency has the effect of physically decreasing/increasing the Kolmogorov length ( $\eta$ ) and time ( $\tau_\eta$ ) scales, and thus the effective resolution:  $\Delta x_p/\eta$ . The simultaneous high  $Re$ , high resolution nature of this data can be seen in Table 1, made notable by the fact that previous works on the morphology of 3D HIT turbulent data have typically been numerical (Buaria & Pumir 2022). Other relevant experimental parameters displayed in Table 1 are defined below.  $\langle \epsilon \rangle$  is an estimate for the average dissipation-rate, found using torque-meters located on the impeller shafts (Kuzzay *et al.* 2015). The integral timescales is  $T_i$ , while the Taylor Reynolds number ( $Re_\lambda$ ) was computed from the measured rms velocity, assuming homogeneity. The relevant frequencies shown are the data acquisition frequency and impeller rotation frequency,  $F_a$  and  $F$  respectively. The ratio of  $\tau_{acf}/\tau_\eta$  is the mean de-correlation time of the time-

resolved velocity fields relative to the Kolmogorov timescale. As this work is statistical and the data acquisition is time resolved, we sample our velocity fields to produce snapshots that are statistically independent temporally. The time-step between independent snapshots is determined by  $\tau_{acf}$ , and the resulting number of statistically independent flow-fields for each case is  $N$ . The autocorrelation function ( $ACF_{ii}(\tau) = \langle v_i(t)v_i(t+\tau) \rangle / \langle v_i^2(t) \rangle$ ) is computed at an array of points in the measurement volume for each, mean subtracted, Eulerian velocity component,  $v_i$ . The de-correlation time  $\tau_{acf}$  is then found via  $\tau_{acf} = \langle ACF(\tau) = 0.025 \rangle$ , or in other words the average de-correlation time of the velocity  $ACF$ .

### 3. Quantities of Interest

The analysis of the experimental data revolves primarily around three quantities and their products. These are the strain-rate tensor  $\mathbf{S}$ , the vorticity vector  $\boldsymbol{\omega}$ , and the scalar parameter “ $\mathcal{D}_\ell$ ” (defined below in Equation 3.3). Again, note that we have sampled the time resolved data to obtain statistically independent data.

Due to their importance in the production of vortex stretching and dissipation, the alignment of  $\boldsymbol{\omega}$  and the principal axes of  $\mathbf{S}$  are of interest. The eigenvectors of  $\mathbf{S}$  ( $\mathbf{e}_1, \mathbf{e}_2, \mathbf{e}_3$ ) have three corresponding eigenvalues which are defined such that  $\lambda_1 \geq \lambda_2 \geq \lambda_3$ . To find the degree of  $\boldsymbol{\omega}$  -  $\mathbf{S}$  alignment, we consider the alignment cosine,  $C_i$ , between the vorticity unit-vector,  $\hat{\boldsymbol{\omega}}$ , and the three principal axes of  $\mathbf{S}$  such that

$$C_i = |\cos(\mathbf{e}_i \cdot \hat{\boldsymbol{\omega}})|. \quad (3.1)$$

$C_i$  is then bounded between 0 and 1 for each principal direction, with  $\boldsymbol{\omega}$  being perpendicular or parallel to  $\mathbf{e}_i$  for values of 0 and 1, respectively.

Incompressible continuity ( $\nabla \cdot \mathbf{u} = 0$ ) imposes an additional constraint on the eigenvalues of  $\mathbf{S}$  such that  $\lambda_1 + \lambda_2 + \lambda_3 = 0$ . Thus, as the most extensive strain eigenvector  $\mathbf{e}_1$  is always positive ( $\lambda_1 > 0$ ) and the most compressive strain eigenvector  $\mathbf{e}_3$  is always negative ( $\lambda_3 < 0$ ), the value of  $\lambda_2$  will change sign depending on the local flow behavior. We quantify the sign and relative amplitude of  $\lambda_2$  using

$$\beta = \sqrt{6}\lambda_2 / \sqrt{\lambda_1^2 + \lambda_2^2 + \lambda_3^2}. \quad (3.2)$$

We will also report statistics on the second and third invariants of the velocity gradient tensor,  $Q$  and  $R$  respectively. Here  $Q = \frac{1}{4}\omega_i\omega_i - \frac{1}{2}S_{ij}S_{ij}$  and  $R = -\frac{1}{3}S_{ij}S_{jk}S_{ki} - \frac{1}{4}\omega_i S_{ij}\omega_j$  - the quantities whose joint distributions make up the aforementioned QR plot. Note that velocity derivatives are computed from the Eulerian field using a second-order central-differencing scheme.

Finally, as we are interested in determining the morphology of the flow field around events which transfer large amounts of energy, we measure this energy transfer using the  $\mathcal{D}_\ell$  parameter, a term generated in the “weak Karman-Howarth-Monin equation” (Dubrulle 2019). This is a scale and space dependent energy balance for the point-split kinetic energy,  $E^\ell(\mathbf{x}) \equiv u_i u_i^\ell / 2$ , developed in previous works by Onsager (1949); Duchon & Robert (2000); Dubrulle (2019).  $E^\ell(x)$  changes across time, space, and scale ( $\ell$ ) due to the transport of energy within the flow. In this work we are only interested in one term from the evolution equation of  $E^\ell(x)$ , the inter-scale energy flux:

$$\mathcal{D}_\ell = \frac{1}{4} \int \nabla \phi^\ell(\boldsymbol{\xi}) \cdot \delta \mathbf{u} (\delta \mathbf{u})^2 d^3 \boldsymbol{\xi}. \quad (3.3)$$

Here the velocity increment, dependent on space ( $\mathbf{x}$ ) and increment-distance ( $\boldsymbol{\xi}$ ), is  $\delta \mathbf{u} = \mathbf{u}(\mathbf{x} + \boldsymbol{\xi}) - \mathbf{u}(\mathbf{x})$ .  $\phi^\ell$  is a smooth, even, non-negative, and spatially localized smoothing

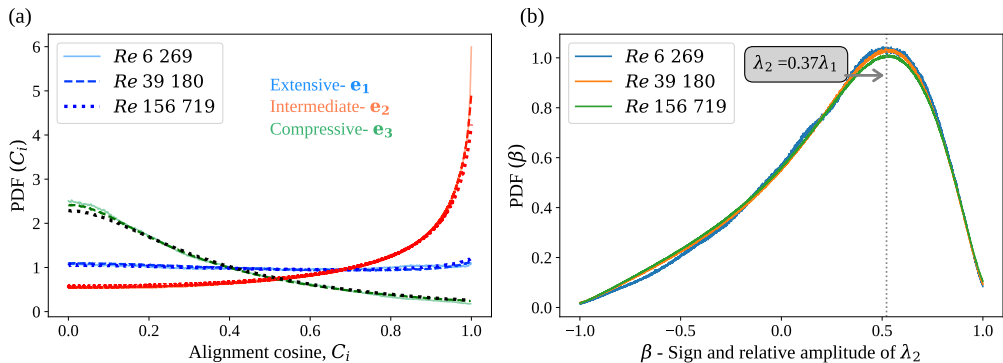


Figure 3: Distributions of  $C_i$  and  $\beta$  for a range of  $Re$ . (a) Alignment cosine ( $C_i$ ) distributions of the strain-rate tensor eigenvectors and the vorticity vector. For each eigenvector, different  $Re$  are indicated by shades of the same color. (b) Distributions of the relative amplitude of the intermediate  $\mathbf{S}$  eigenvector ( $\beta$ ) for different  $Re$ . The value of  $\lambda_2$  (relative to  $\lambda_1$ ) corresponding to the most probable  $\beta$  value is shown in the gray box.

operator which effectively removes fluctuations on scales smaller than  $\ell$ , meaning smaller  $\ell$  results in less smoothing. In our case it is the following Gaussian function:  $\phi^\ell(x) = \exp\left(-\frac{30x^2}{2\ell^2}\right) / \left(\frac{2\pi\ell^2}{30}\right)^{1.5}$ . The scalar  $\mathcal{D}_\ell$  is the non-viscous inter-scale transfer term, *i.e.* the local (in space and time) rate of energy transfer from scales larger than  $\ell$  to scales smaller than  $\ell$ . It adopts the convection that positive  $\mathcal{D}_\ell$  values indicate energy transfer to scales below  $\ell$  and vice-versa (Dubrulle 2019; Debye *et al.* 2021). In the limit of  $\ell \rightarrow 0$ ,  $\mathcal{D}_\ell$  can also be thought of as an inertial dissipation arising from the irregularity of the velocity field, or in other words, the non-viscous contribution to dissipation due to velocity roughness (Duchon & Robert 2000).

## 4. Results

### 4.1. Unconditioned Statistics

Figure 3 shows the unconditioned probability density functions (PDFs) of the alignment cosine ( $C_i$  - Equation 3.1) and the intermediate eigenvector sign and amplitude ( $\beta$  - Equation 3.2) for a range of  $Re$ . The results agree well with the vast amount of previous works, a majority of which were done using DNS on HIT flows. We observe the common trend of  $\omega$  alignment with the intermediate  $\mathbf{S}$  eigenvector, which is generally positive (extensive). We also observe the lack of any preferential alignment with the extensive eigenvector ( $e_1$ ) and a preference for perpendicularity between  $\omega$  and  $e_3$ , the principal compressive axis of  $\mathbf{S}$ . See Figure 1a for a schematic showing this preferred nominal alignment of an idealized vortex in a strain field. While the preference for  $\lambda_2 > 0$  was shown by Betchov (1956) to be necessary for net enstrophy-production in a turbulent flow, the predominant  $\omega - e_2$  alignment has been used to explain the limited vorticity growth rates, as compared to those of passive scalars, observed in turbulence (Elsinga & Marusic 2010).

The unconditioned joint PDF of the velocity-gradient invariants  $Q$  and  $R$  for the case of  $Re = 156719$ , scale  $\ell = 6.5\eta$ , are shown in the QR plot of Figure 4. Again due to incompressibility, the first invariant,  $P$ , of the velocity gradient is zero. As such, one can define a line ( $D$ ) which separates the real and complex roots of the velocity-gradient tensor as:  $D = Q^3 + (27/4)R^2$ . Meaning that  $D > 0$  represents swirling flow topology, while regions with  $D < 0$  are strain dominated. This is shown as the dashed line in Figure 4 and

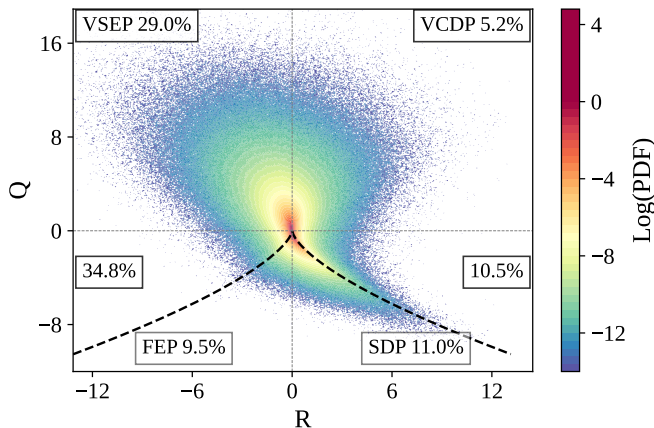


Figure 4: QR plot of the non-conditioned turbulent flow at  $Re=156\,719$ . The dashed line is the Vieillefosse line. VSEP (Vortex-Stretching Enstrophy-Production), VCDP (Vortex-Compressing Dissipation-Production), SDP (Sheet Dissipation-Production) and FDP (Filament Enstrophy-Production) indicate different topological regions of QR space. The percentage of total events in each region are also indicated by the text boxes. The plots have been non-dimensionalized using the appropriate powers of  $\langle S_{ij}S_{ij} \rangle$ .

is better known as the “Vieillefosse line/tail”(Vieillefosse 1984). The QR plot can be further partitioned based on the sign of  $R$  and  $Q$ , where positive and negative  $R$  indicate unstable and stable solutions, respectively, while positive and negative  $Q$  indicate enstrophy dominated and strain dominated regions, respectively (Chevillard & Meneveau 2006; Chevillard *et al.* 2008; Elsinga & Marusic 2010). One can also interpret the sign of  $R$  morphologically, where  $R < 0$  indicates a stretching principal direction (i.e vortex-stretching) and  $R > 0$  indicates a compressive principal direction (strain-self-amplification or vortex-compression).

The QR plot can therefore be divided into 4 (or 6) regions, each corresponding to a solution-type of the characteristic equation of the velocity-gradient tensor’s eigenvalues, which correspond to different flow topologies. The top left region of the QR plot in Figure 4 labeled VSEP (Vortex-Stretching Enstrophy-Production:  $R < 0, Q > D$ ) is characterized by enstrophy producing regions of the flow driven by stable vortex-stretching topologies. The top right region labeled VCDP (Vortex-Compressing Dissipation-Production:  $R > 0, Q > D$ ) contains regions of the flow that produce dissipation via unstable vortex-compression topologies. Correspondingly, the bottom right region labeled SDP (Sheet Dissipation-Production:  $R > 0, Q < D$ ) pertains to unstable saddle-node, or sheet, topologies which tend to produce dissipation. Finally, the bottom left region labeled FEP (Filament Enstrophy-Production:  $R < 0, Q < D$ ) produces enstrophy via stable-node, or filament topologies (Debue *et al.* 2021; Chong *et al.* 1990; Chevillard & Meneveau 2006; Chevillard *et al.* 2008; Elsinga & Marusic 2010; Danish & Meneveau 2018). We direct the reader to the work of Suman & Girimaji (2010) for a more nuanced explanation of stability/instability in the QR plot. One can additionally split the VSEP and VCDP regions into  $Q > 0$  and  $0 > Q > D$  where the former contains swirling topologies in regions dominated by enstrophy, and the latter, while still containing swirling topologies, are regions where strain is more prevalent (Danish & Meneveau 2018).

The resulting tear-drop shape of the QR plot (with the pointed portion along the positive/right Vieillefosse tail) in Figure 4 is now one of the most notable features in a turbulent flow (Elsinga & Marusic 2010). This familiar shape indicates that, on average,

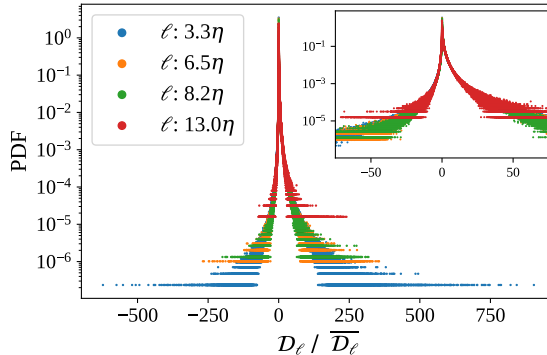


Figure 5: PDFs of mean-normalized energy transfer ( $\mathcal{D}_\ell$ ) to and from scale  $\ell$  for a range of scales at  $Re=156\,719$ . The mean to RMS ratio of  $\mathcal{D}_\ell$  at each scale are as follows:  $3.3\eta$  -  $0.0032/0.0167$ ,  $6.5\eta$  -  $0.0106/0.0421$ ,  $8.2\eta$  -  $0.0147/0.0542$ ,  $13.0\eta$  -  $0.0255/0.2242$ .

turbulent flows generate enstrophy via vortex-stretching and produce dissipation via sheets and compressive vortices in strain dominated regions. The ubiquity of the results shown in Figures 3 and 4 may be interpreted as universal statistical manifestations of the structure of turbulent flows (Tsinober 2009). Additionally, one should note that a random, divergence-free flow field would result in a shape symmetric about the R axis (Elsinga & Marusic 2010), which is of course not the case here, highlighting the very non-Gaussian nature of turbulence.

Finally, we quantify the scale-to-scale energy transfer in our flow using  $\mathcal{D}_\ell$ , previously defined in Equation 3.3. The distribution of  $\mathcal{D}_\ell$  is shown in Figure 5 for a range of scales at the highest  $Re$  (156 719). One can see the highly non-Gaussian nature of the distribution, as the long tails indicate energy transfer events up to three orders of magnitude higher than the mean. Three things should be noted regarding Figure 5. The first is that the relative amplitudes of the largest events increase as the scale decreases. Second, positive values of  $\mathcal{D}_\ell$  (which we will call  $\mathcal{D}_\vee$ ) indicate “direct” cascade or downscale energy transfer events, while negative values ( $\mathcal{D}_\wedge$ ) indicate “inverse” cascade or upscale energy transfer events. One should also note the PDF of  $\mathcal{D}_\ell$  is skewed towards positive values for each scale. This shows that  $\langle \mathcal{D}_\ell \rangle > 0$ , which is of course a manifestation of the turbulent cascade - on average, energy flows from larger scales to smaller scales. Lastly, we highlight the scale size indicated in terms of  $\eta$  in the legend of Figure 5. It is postulated that the transition between the inertial and viscous range occurs in the range of  $10$ - $20\eta$ , placing this work squarely at or below this regime (Danish & Meneveau 2018).

#### 4.2. Statistics conditioned on extreme energy transfer

The results presented in Figures 3-5 were produced by sampling the whole flow field. As such, they do not distinguish between intermittent and quiescent regions, or areas of upscale and downscale energy transfer. To determine the morphology of the flow during the largest amplitude energy transfers we bin the flow field by decades of positive/negative  $\mathcal{D}_\ell$ , and then calculate the local  $\omega$  -  $\mathbf{S}$  alignment at all points in each respective  $\mathcal{D}_\ell$  bin. Here we consider extreme/large energy transfer events to be those with amplitudes between  $100$ - $1000$  times the respective means of  $\mathcal{D}_\wedge$  and  $\mathcal{D}_\vee$ . Note that, unless explicitly noted, the conditioning was done for the case of  $Re = 156\,719$  at scale  $\ell = 6.5\eta$  as this case provided the most converged statistics. Thus we will drop the  $\ell$  from the subscript of  $\mathcal{D}_\ell$ .

Figure 6a shows the alignment cosine  $C_i$  conditioned on downscale energy events satisfying  $100$ - $1000\mathcal{D}_\vee$ . The conditioned probabilities of  $C_i$  (solid-bold lines) are shown along with

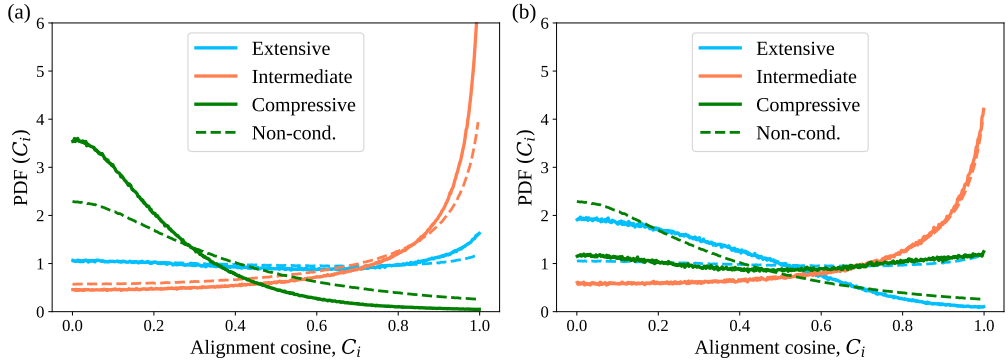


Figure 6: Alignment cosine,  $C_i$ , conditioned on large magnitude events of downscale and upscale energy transfer. (a)  $C_i$  of  $\omega - \mathbf{S}$  at areas of the flow field with large ( $> 100\overline{\mathcal{D}}_V$ ) downscale transfer. (b)  $C_i$  of  $\omega - \mathbf{S}$  at areas of the flow field with large ( $> 100\overline{\mathcal{D}}_\Lambda$ ) upscale transfer. (a-b) Conditioned probabilities for each eigenvector (solid-bold lines) are shown compared to their respective unconditioned alignments (dashed-thin lines).

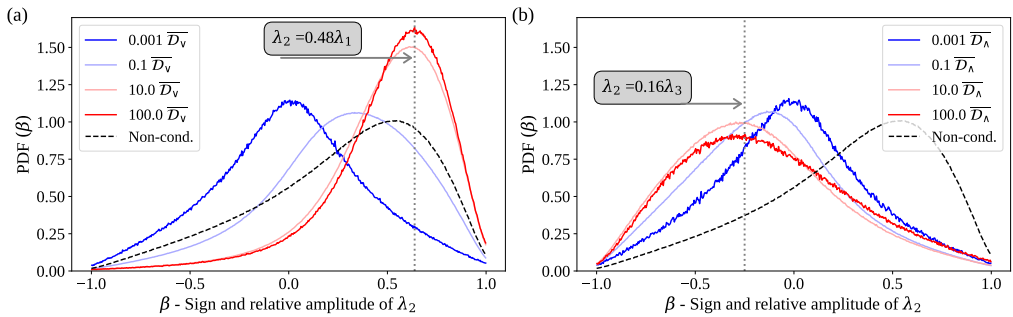


Figure 7: Evolution of the  $\beta$  distribution when conditioned on varying levels of downscale (a) and upscale (b) energy transfer amplitude. Conditioning level varies between events of (a) 0.001-100 $\overline{\mathcal{D}}_V$  and (b) 0.001-100 $\overline{\mathcal{D}}_\Lambda$ , from the smallest (bold blue line) to largest (bold red line). The black dashed line is the non-conditioned result. The value of  $\lambda_2$  (relative to  $\lambda_1$  (a) or  $\lambda_3$  (b)) corresponding to the most probable  $\beta$  is shown in the gray text box.

the respective unconditioned alignments (dashed-thin lines). One can see that for large magnitude direct cascade events, the unconditioned  $\omega - \mathbf{S}$  alignment is enhanced. That is to say,  $\omega$  aligns more strongly with  $\mathbf{e}_2$  and has a larger preference for perpendicularity with  $\mathbf{e}_3$ . Although there is a slight increase in the propensity for  $\mathbf{e}_1$  to align with  $\omega$ , by and large it remains preferentially unaligned. It is particularly notable that the propensity for perpendicular alignment of  $\omega - \mathbf{e}_3$  nearly doubles for the largest direct cascade events.

Additionally, Figure 7a shows the distribution of  $\beta$  for a range of conditioning levels, from 0.001-100  $\overline{\mathcal{D}}_V$ . The lowest magnitude downscale energy transfer produces a normal-like distribution in  $\beta$  with no preference for compressive or extensional  $\mathbf{e}_2$ . The distribution of  $\beta$  gradually shifts rightward as the level of conditioning on  $\overline{\mathcal{D}}_V$  increases, such that at the largest downscale transfers ( $> 100 \overline{\mathcal{D}}_V$ )  $\mathbf{e}_2$  is almost entirely extensional. There is also a notable increase in the most probable magnitude relative to  $\lambda_1$  (from  $0.37\lambda_1$  to  $0.48\lambda_1$ ), as indicated by the gray text boxes in Figures 3b and 7a.

The alignment statistics conditioned on upscale energy transfer,  $\overline{\mathcal{D}}_\Lambda$ , are shown in Figures 6b and 7b. The  $\omega - \mathbf{S}$  alignment is shown in Figure 6b, where the  $\omega - \mathbf{e}_2$  alignment is

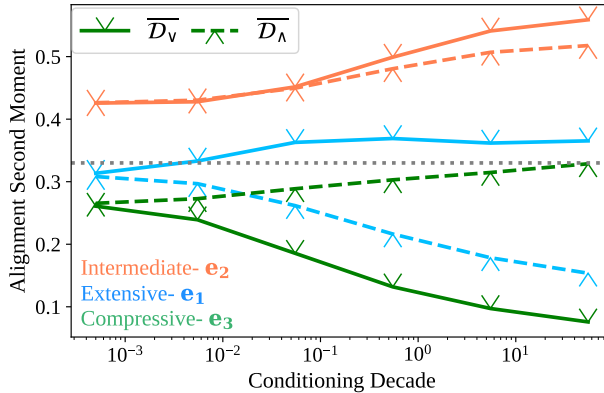


Figure 8: Average second moment of the alignment cosine across a range of increasing amplitude downscale ( $\overline{\mathcal{D}}_V$ - solid lines) and upscale ( $\overline{\mathcal{D}}_\Lambda$ - dashed lines) energy transfer conditioning levels. The faint, dotted gray line is at  $1/3$ , which corresponds to uniform distributions of  $C_i$ . Values closer to 0 or 1 indicate average perpendicular or parallel  $\omega - \mathbf{e}_i$  alignment, respectively.

shown to be effectively identical to the non-conditioned case. However, notably it displays a preference for orthogonality with the extensive  $\mathbf{e}_1$ , instead of the compressive  $\mathbf{e}_3$  as in the non-conditioned case.

The evolution of the  $\beta$  distribution is again shown, but for increasing upscale transfers (0.001-100  $\overline{\mathcal{D}}_\Lambda$ ) in Figure 7b. Once again, we note the effectively normal distribution of  $\beta$  values for the smallest  $\overline{\mathcal{D}}_\Lambda$  events. However, as the conditioning level increases, the distribution of  $\beta$  moves leftwards to negative values. At the largest upscale energy transfers,  $\beta$  is primarily negative (compressive), albeit with a wider distribution that includes a sizable amount of positive  $\lambda_2$ . The relative magnitude of  $\lambda_2$ 's most probable value as compared to its complimentary eigenvalue ( $\lambda_3$  in this case) has also decreased compared to the non-conditioned case - from  $0.37\lambda_1$  to  $0.16\lambda_3$ .

A notable feature that applies to both the direct and inverse cascade cases, is that  $\omega$  always shows a preferentially perpendicular alignment with the largest magnitude eigenvector, or the direction of highest amplitude strain. For  $\overline{\mathcal{D}}_V$ , as  $\lambda_2 > 0$ ,  $\omega$  is most perpendicular to  $\mathbf{e}_3$  (because  $\lambda_1 + \lambda_2 = \lambda_3$ ). While for  $\overline{\mathcal{D}}_\Lambda$ ,  $\omega$  is preferentially orthogonal to  $\mathbf{e}_1$  in the inverse cascade as  $\lambda_1 = \lambda_2 + \lambda_3$ .

In order to gauge how the alignment might change across different energy amplitudes we investigate the average second moment of the alignment cosine,  $\langle (\mathbf{e}_i \cdot \hat{\omega})^2 \rangle$ . This variable is useful in that it is bounded between 0 and 1, and the sum of the three contributing directions will also sum to 1. The value for each eigenvector gives an idea of the average alignment for the distribution of  $C_i$  at each conditioning level. Its average value conditioned on varying levels of up/downscale energy transfer is shown in Figure 8. One can see that at the highest conditioning levels we recover the results of Figure 6, where there is greatest preference for  $\omega - \mathbf{e}_2$  alignment and a orthogonal preference which swaps between  $\mathbf{e}_3$  for  $\overline{\mathcal{D}}_V$  events (downscale - solid lines) and  $\mathbf{e}_1$  for  $\overline{\mathcal{D}}_\Lambda$  events (upscale - dashed line). If we note that a eigenvector with no alignment preference (uniformly distributed) will have a value  $\langle (\mathbf{e}_i \cdot \hat{\omega})^2 \rangle = 1/3$  we can make a surprising observation. This is the fact that at the lowest energy transfer levels, the average  $\omega - \mathbf{S}$  alignment seems to maintain a morphological structure. This is surprising as several works have found that  $\langle (\mathbf{e}_i \cdot \hat{\omega})^2 \rangle$  conditioned on lowest levels of

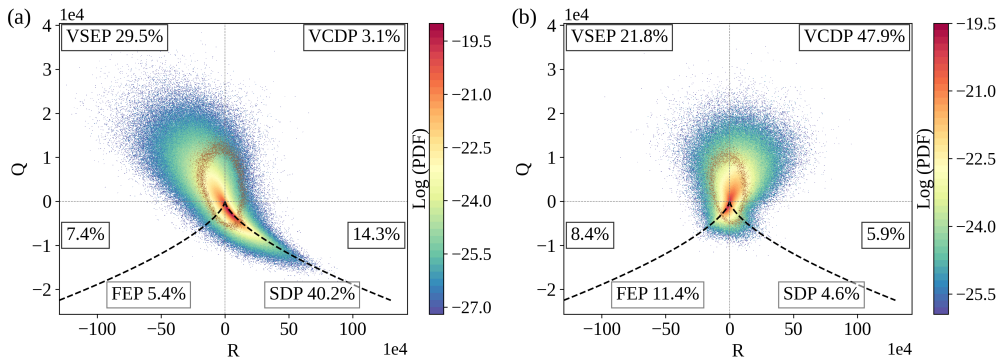


Figure 9: QR plots conditioned on large magnitude (a) downscale ( $> 100\overline{\mathcal{D}}_v$ ) and (b) upscale ( $> 100\overline{\mathcal{D}}_\lambda$ ) energy transfer events. The faint-red ring of scatter-points in the center of each figure shows the outer contour-level for the QR plot conditioned on the mean (a) direct and (b) inverse cascade. The percentage of events located in each labeled region (acronyms defined previously in the text and Figure 4) are indicated in the text boxes. The dashed line is the Vieillefosse line. The plots have been non-dimensionalized using the appropriate powers of  $\langle S_{ij}S_{ij} \rangle$ .

entropy or strain will converge to  $1/3$  for all eigenvectors (Buaria *et al.* 2020). This perhaps points to the fact that energy transfer is more inherently linked to morphological structure.

We next use the conditioned statistics to generate QR plots for the largest upscale and downscale energy transfer. Figure 9a shows the QR plots for downscale energy transfers  $> 100\overline{\mathcal{D}}_v$ . While the resulting tear drop is similar to the non-conditioned case, it is considerably more elongated along the Vieillefosse line. Thus, a vast majority of its events are in the VSEP region, where vortex-stretching is prominent, and in the sheet forming dissipation producing regions, SDP. The large downscale energy transfer events also pull the pointed portion of the tear drop further down the right Vieillefosse tail, particularly for the most probable events. In regards to the non-conditioned QR plots the greatest changes are in the SDP region (11% to 40%) and the enstrophy-producing non-swirling region (35% to 7%).

Alternatively, Figure 9b shows the QR plot for upscale energy transfers  $> 100\overline{\mathcal{D}}_\lambda$ . The tear drop for the inverse cascade is shown beginning to tilt along the opposite Vieillefosse left tail. In this case there are proportionately many more events in the VCDP region, corresponding to vortex-compression topology. Additionally, while there is a slight hitch remaining along the right Vieillefosse tail, the most probable events are oriented along the left tail. In regards to the non-conditioned QR plot the greatest changes occur in the VCDP region (5% to 48%), the two regions around the right Vieillefosse tail (totals of 20% to 11%) and again in the enstrophy-producing non-swirling region above the left Vieillefosse tail (35% to 8%). It should be noted that because net energy transfer is downward, there are fewer statistics for both the inverse cascade as a whole and for large amplitude upscale events, as compared to their downscale counterparts. Thus we have found that the  $\overline{\mathcal{D}}_v$  is typically 2.5 times larger than the amplitude of  $\overline{\mathcal{D}}_\lambda$ .

Comparatively, in the downscale case most events are in the regions of enstrophy-production via vorticity (VSEP) and dissipation-production via strain (SDP). However in the upscale case, while there is still vortex-stretching producing enstrophy, there is also a notable amount of enstrophy-production via straining and filaments (FEP). Interestingly, dissipation-production is now primarily due to vortex-compression (VCDP). Furthermore, as noted previously there exists a much higher degree of nonlinearity in the direct cascade as opposed to

the inverse cascade (Tsinober 1998, 2009). As these nonlinearities are highly correlated with strain dominated ( $2S_{ik}S_{ik} > \omega^2$ ), and strain producing regions ( $-S_{ik}S_{km}S_{mi} > 3/4\omega_i\omega_kS_{ik}$ ) the largest downscale energy transfer may be highly nonlinear due to the preponderance of events along the right tail of Figure 9a.

## 5. Discussion

### 5.1. Contribution of Individual Eigenvectors

Understanding the amplitude and direction of each eigenvector is crucial for delineating the contributions of vortex-stretching and strain-rate to large amplitude energy transfer. These contributions can be better understood by examining the governing equations for the enstrophy,  $\Omega$ , and an estimate of the dissipation rate,  $\Sigma$ , (where  $\Sigma = 2S_{ij}S_{ij}$  and the local dissipation rate is  $\epsilon = \nu\Sigma$ ), both shown here:

$$\frac{1}{2} \frac{D\Omega}{Dt} = \underbrace{\omega_i^2 \lambda_i \cos^2(\omega, \mathbf{e}_i)}_{\text{VS}} + \nu \omega_i \nabla^2 \omega_i, \quad (5.1)$$

$$\frac{1}{2} \frac{D\Sigma}{Dt} = - \underbrace{(\lambda_1^3 + \lambda_2^3 + \lambda_3^3)}_{\text{SSA}} - \frac{1}{4} \underbrace{\omega_i^2 \lambda_i \cos^2(\omega, \mathbf{e}_i)}_{\text{VS}} - S_{ij} \frac{\partial^2 p}{\partial x_i \partial x_j} + \nu S_{ij} \nabla^2 S_{ij}. \quad (5.2)$$

Above we have neglected external forcing and replaced the vortex-stretching (VS =  $\omega_i\omega_jS_{ij}$ ) and strain-self-amplification terms (SSA =  $S_{ij}S_{jk}S_{ki}$ ) with equivalent terms based on the eigenvalues of  $\mathbf{S}$  (Tsinober 2009; Buaria & Pumir 2021).

From Equation 5.1 we can see that only the first term on the RHS (the vortex-stretching term) is a source of  $\Omega$  production, and this is only the case when  $\lambda_i > 0$ . Additionally, the contribution from each eigenvector depends on both the alignment and the magnitude. The VS term also occurs in Equation 5.2 as a sink, albeit with three quarters less effect. Thus, in this case when  $\lambda_i > 0$ , the vortex-stretching term opposes dissipation-production, while it creates dissipation when  $\lambda_i < 0$ .

Alternatively, the first term on the RHS of Equation 5.2 is the strain-self-amplification term, which produces dissipation only if two eigenvalues are positive. This has two important implications, the first being that due to incompressibility  $\lambda_1 + \lambda_2 + \lambda_3 = 0$ , and in the situation where  $\lambda_1, \lambda_2 > 0$ , the only term contributing to the production of dissipation through SSA is the compressive strain eigenvector  $\mathbf{e}_3$  (Gulitski *et al.* 2007). One should also note that in this case ( $\lambda_2 > 0$ ), the larger the magnitude of  $\lambda_2$ , the larger the SSA, as  $\lambda_1 \approx \lambda_2$  minimizes their respective negative contributions, due to the cubed powers in Equation 5.2. Second, it is not possible to produce dissipation through the SSA term when  $\lambda_2 < 0$  as only two positive eigenvalues yield a positive number, and by definition  $\lambda_1 > 0$  and  $\lambda_3 < 0$ . This can be observed in our data in Figure 10, as the SSA term conditioned on the inverse cascade (SSA| $\overline{\mathcal{D}_\lambda}$ ) begins to destroy dissipation once the upscale energy amplitude reaches a level where the distribution of  $\lambda_2$  skews negative (see  $\beta$  in Figure 7b). This fact demonstrates that the compressive action of  $\mathbf{e}_3$  alone is what skews  $\langle S_{ij}S_{jk}S_{ki} \rangle$  negative, and because this term is proportional to the distribution of velocity derivatives, it's also responsible for their negative skewness. In other words, the compression of  $\mathbf{e}_3$  results in the negative skewness of longitudinal velocity increments, a hallmark of the intrinsic non-Gaussian structure of turbulent statistics, and an exact result of Kolmogorov 4/5ths law (Rosales & Meneveau 2006). This suggests that because we observe a generally negative  $\lambda_2$  (Figure 7b) in the

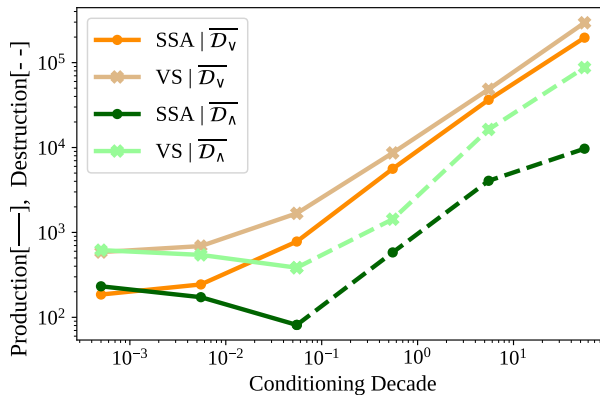


Figure 10: Average vortex-stretching (VS in Equation 5.1) and strain-self-amplification (SSA in Equation 5.2) terms conditioned on increasing amplitudes of direct ( $\overline{\mathcal{D}}_V$  - orange hues) and inverse ( $\overline{\mathcal{D}}_\Lambda$  - green hues) cascade events. Dashed portions of the lines represent destruction of the respective quantity. Pale hues show VS, while deeper colors are SSA.

inverse cascade case, longitudinal velocity increments should skew less negatively for large upscale energy transfer.

The average values of the VS and SSA terms in Equations 5.1 and 5.2 are shown for different levels of direct and inverse cascade conditioning in Figure 10. For the direct cascade case, both VS and SSA increase as a power-law dependent on the energy transfer amplitude. However, in the case of inverse cascade, these terms both decrease as upscale amplitude increases, until the point where they actually become net sinks of enstrophy and dissipation (as indicated by the dotted lines in Figure 10).

Understanding the contributions to the VS term are more complicated due to the simultaneous dependence on alignment, sign, and amplitude. Thus we show the average individual contributions of each eigenvector to enstrophy-production via the normalized vortex-stretching term in Figure 11. One can see that in the direct cascade case of Figure 11a, the  $e_2$  contribution grows steadily with increasing energy transfer amplitude until the largest events where it nearly matches the contribution from  $e_1$ . Notably,  $e_1$  is shown to still contribute majorly despite the preference of  $\omega - e_2$  alignment, at least in the average sense. Concerning the inverse cascade (Figure 11b), we see that once the mean conditioning level is reached, there is actually a net destruction of enstrophy due to VS (as the negative contributions crosses the white 50% line). Further, the relative contribution of  $e_2$  remains small for all conditioning levels and the vortex-stretching term in the inverse cascade is dominated by the most extensive and compressive eigenvectors, despite the preference for  $\omega - e_2$  alignment.

### 5.2. Importance of Strain vs. Vortex Stretching

If we return to the conditioned  $\beta$  statistics (Figure 7), during the largest direct cascade events the relative magnitude of  $\lambda_2$  increases from 37% of  $\lambda_1$  in the non-conditioned statistics to nearly 50%. Coupled with the stronger degree of  $\omega - e_2$  alignment, this indicates a very large contribution from  $e_2$  to the velocity-gradient dynamics, as we have already remarked in Figure 11a. One can also see the near total absence of negative(compressive)  $\lambda_2$  for the largest direct cascade events (Figure 7a), which can also be observed in the corresponding QR plot of Figure 9a. This manifests such that there are merely 3% of all events located in the vortex-compressing region VCDP. Additionally, simultaneous  $\omega$  alignment with  $e_2$  and

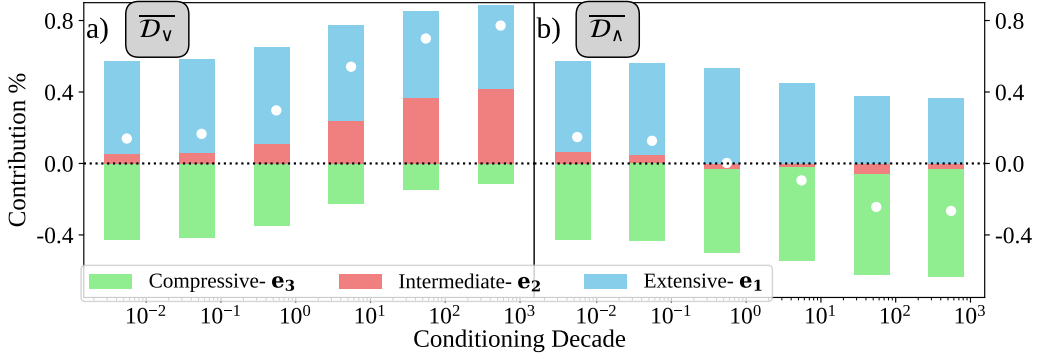


Figure 11: Normalized contributions of each  $\mathbf{S}$  eigenvector towards the vortex-stretching (VS) term in Equation 5.1 conditioned on increasing amplitudes of (a)  $\overline{\mathcal{D}_v}$ - downscale and (b)  $\overline{\mathcal{D}_\lambda}$ - upscale energy transfer. The bars shown are all the same normalized height, and the size/contribution of each eigenvector is found by dividing the absolute value of the eigenvalue contribution by the absolute value sum of all the contributions. The eigenvalue contributions which contribute negatively are shown below the x-axis. The white dot signifies the net normalized sum of the contributions

orthogonality with a large magnitude compressive  $e_3$  indicates morphology that is more akin to strain-self-amplification (*i.e.* Figure 1b) than vortex-stretching. This is indeed observed in the QR plot as over 50% of events are found along the right Vieillefosse tail.

In Figure 7b, for the largest inverse cascade events,  $\beta$  has the reverse trend, where the relative amplitude of  $\lambda_2$  decreases from 37% of  $\lambda_1$  to 16% of  $\lambda_3$ . Meaning that for the largest upscale events the compressive and extensive eigenvectors have very big relative amplitudes and dominate the strain magnitude, despite the domination of  $\omega - e_2$  alignment. One can see the link between the inverse cascade QR plot of Figure 9b and Figure 7b by noting the relatively wide distribution of  $\beta$  during the largest events. Because there is a large number of positive and negative values of  $\lambda_2$ , this manifests in the QR plot as a plethora of events in both the vortex-stretching (VSEP) and compressing (VCDP) regions.

Therefore we posit that because there is a comparable number of vortex-stretching topologies in the VSEP region for both the direct (30% in Figure 9a) and inverse (22% in Figure 9b) cascade, vortex-stretching is not the primary factor in determining cascade direction. Instead it is the number of vortex-compressing events (only 3% in downscale vs 50% in upscale) and strain-self-amplification events (over 50% in downscale and under 10% in upscale) that mark the key phenomenological differences in cascade direction. Additionally, one can see the most probable values of the large amplitude inverse cascade beginning to orient along the left Vieillefosse tail in Figure 9b.

More generally, these results seem to add credence to the idea that the role of vorticity in the energy cascade is overblown (Tsinober 1998; Carbone & Bragg 2020; Johnson 2020; Vela-Martín & Jiménez 2021). The most obvious sign of this is seen in Figure 9, as was just discussed above. The eigenvector directionality for the inverse ( $\lambda_3, \lambda_2 < 0$ ) and direct ( $\lambda_1, \lambda_2 > 0$ ) cascades found in this work also agree with that found in Vela-Martín & Jiménez (2021). This result shows that downscale energy transfer is much more likely to have self-strain-amplification due to its single negative eigenvector. While the largest upscale energy transfer events show a repulsion for straining topologies - only around 15% of all events exist below the Vieillefosse lines in Figure 9b. However, a notable departure between this work and that of Vela-Martín & Jiménez (2021) is our observation that the number of vortex-

compressing events varies drastically between the large amplitude direct and inverse cascade. The aforementioned numerical work (large eddy simulation) showed vortex compression to exist in large quantities for both directions. We posit that this difference is primarily due to two factors, the first being that our statistics concern scales ( $6.5\eta$ ) much smaller than the large scales explicitly resolved in their work. Second, our statistics are conditioned on the largest energy transfer events, whereas their work artificially forced the average flow of energy to be up or downscale.

### 5.3. Morphology and Singularity Aspects

Recalling aspects of the discussion above can give us an idea on the vortex morphology during large amplitude energy transfer events. Considering that during the largest downscale events, we observe 1) high positivity of  $\lambda_2$ , 2) relatively large magnitude  $\lambda_2$  as compared to  $\lambda_1$ , and 3) a strong preference for orthogonality between  $\omega - e_3$  we see a mechanism for the formation of sheet like structures. The vortex, being well aligned with a large amplitude  $e_2$ , is compressed strongly by the largest amplitude eigenvector  $e_3$ , and simultaneously pulled strongly by  $e_2$  and  $e_1$ . This straining mechanism, illustrated in Figure 1b, is associated with the squeezing of fluid elements into sheet-like structures and has been observed in previous works in flow-regions with high vorticity (Vincent & Meneguzzi 1994; Rosales & Meneveau 2006). The formation of these sheets can then induce shearing instabilities that in turn cause roll up of the compressed vortex sheets. The fact that the most populous region of the QR plot in this case is along the Vieillefosse right tail perhaps signals that quasi-singularities may be associated with vortex-sheet morphology more so than those of vortex tubes.

We must also consider that this dominant alignment in the direct cascade case was shown by Vieillefosse (1982); Cantwell (1992) to cause Restricted-Euler singularities in the velocity-gradient along the right Vieillefosse tail. Notably, we not only see this form accentuated for the largest downscale energy transfer events, but also an elongation of the tear-drop shape along the right Vieillefosse tail in Figure 9a. Similar elongation have been previously found for increases in  $Re$  (Chevillard & Meneveau 2006). For the largest amplitude direct cascade transfers, a majority of events are clustered in this region where singularities are expected to occur. This may lend credence to the idea that quasi-singularities, or large non-linearities events in the velocity field (shown to occur in greater proportions in this area (Tsinober 1998, 2009)) might be associated with the largest downscale energy transfer events. Our results also support the prediction of Vieillefosse (1982) that this region along the right tail should have large negative strain skewness. One can see this in two ways, first by observing the power-law increase of SSA for increasing amplitude of direct cascade in Figure 10. Second, by recalling the increase of  $\lambda_2$  relative to  $\lambda_1$  for the largest downscale energy transfer events in Figure 7a. Which, because of incompressibility ( $\lambda_3 = \lambda_1 + \lambda_2 \approx 1.5\lambda_1 \approx 3\lambda_2$ ) and the cubed powers in the SSA term of Equation 5.2 (as already explained in Section 5.1), causes the increasing dominance of the negative contribution to strain coming from  $\lambda_3$ . This further associates strain skewness with energy transfer. Additionally, the increasing number of events along the Vieillefosse tail for increasingly large downscale transfer events, perhaps signals that the energy cascade is piloted by Euler restricted (singular) dynamics.

However, while an increase of events along the Vieillefosse tail points to an increase in the velocity-field non-linearities, the dominant morphology may simultaneously point towards the opposite conclusion. For the largest downscale events we noted the enhanced parallel and perpendicular alignment between  $\omega - e_2$  and  $\omega - e_3$  respectively. In other words, this alignment gives evidence for quasi-2D structures where  $\omega$  is increasingly parallel to the intermediate strain direction while the other two eigenvectors lie in the equatorial plane. This behavior has also been observed previously, but for extreme events in enstrophy, not energy cascade (Jiménez 1992; Buaria *et al.* 2020). This should in turn lead to a reduction in the

non-linearity, as the terms  $\omega_i\omega_j S_{ij}$  and  $\omega_i S_{ij}$  both vanish for 2D flows (Tsinober 2009). This would indicate a higher degree of non-linearity during inverse cascade events than in direct cascade events, a conclusion in contrast to that drawn from the QR plots. However, one could argue that although an increased two dimensionality may inhibit non-linearities induced by the interaction of velocity and vorticity, non-linearities existing due to the so called “turbulent pressure” can still exist and even increase. Clearly further work is needed to more explicitly quantify and investigate “non-linearities” in the velocity field.

We close by discussing perhaps the most interesting finding of this work. If we return our attention to Figure 9, one should focus on the red portion of the contour plots indicating the location of the most probable events. It is notable that these events hug the left (Figure 9b) and right (Figure 9a) Vieillefosse tails for the upscale and downscale cases, respectively. In other words, most large magnitude upscale and downscale energy transfer events are approximately symmetric about the R-axis; a signature of symmetry under time reversal ( $t \rightarrow -t$ ,  $\mathbf{u} \rightarrow -\mathbf{u}$ ). This is noteworthy because the governing Navier-Stokes equations (NSE) should only be invariant in the inviscid limit (Dubrulle 2019). While the same R-axis symmetry has been observed in the aforementioned work of Vela-Martín & Jiménez (2021), it was at large scales, where viscosity can be more readily neglected. However in the current work, we are presenting results just above Kolmogorov’s dissipative scale ( $6.5\eta$ ); clearly close enough that viscosity ought to break symmetry in the NSE. All the same, around events which transfer large amounts of energy up and down scale, we observe evidence of time reversal symmetry. It is hypothesized that this is because the flow is inertially dominated in the space surrounding these events, allowing for the assumption of inviscid-ness even at such small scales.

#### 5.4. Future Work

Further work is needed to investigate whether there exists a type of universal scaling for extreme events in energy transfer, enstrophy, and strain, such as in Buaria & Pumir (2022). An investigation such as this would be useful in determining the validity of the multifractal model of turbulence. It is also of interest to better determine how the cascade is linked to intermittency, and how morphologies of velocity-gradients might change based on their location in or outside of intermittent regions. We have the ability to probe this as previous works have used the  $\mathcal{D}_\ell$  parameter to spatially identify regions of high intermittency (Dubrulle 2019). Further, a study of the turbulent statistics for only upscale energy transfer regions is in order, as there are several properties worth investigating such as the change in skewness of the longitudinal velocity increments. We must also address the issue of scale. While the conditioned statistics presented here were for one specific scale ( $\ell = 6.5\eta$ ), it is not known how morphology may change as we approach or exceed the Kolmogorov scale. Additionally, for an extreme energy transfer at one scale, it is important to know whether there are imprints of this event felt at scales above/below it. Finally, it is of great interest to know how the pertinent morphologies found in this work compare to those generated during vortex-reconnection, as this is another mechanism possibly linked to singularities and extreme energy transfer (Yao & Hussain 2020, 2021).

**Acknowledgements.** The authors thank Cécile Wiertel-Gasquet for her countless efforts in the coordination and execution of the experiments, as well as her patience with the first author. They also thank Vincent Padilla for his practical wizardry and quick problem solving. Thanks are also due to Alain Pumir for useful discussions on the interpretation of these results. Erin Wilson also deserves thanks for her assistance with the schematics in this work. Finally, the authors are immensely thankful to Mauro Abella for his freight elevator rescue and enjoyable lunchtime discussions.

**Funding.** This work received support from the Ecole Polytechnique, CNRS, from ANR TILT (grant No. ANR-20-CE30-0035) and from ANR BANG (grant No. ANR-22-CE30-0025). This project has also

received funding from the European Union's Horizon 2020 research and innovation program under the Marie Skłodowska-Curie grant agreement No. 945298.

**Declaration of interests.** The authors report no conflict of interest.

**Author ORCIDs.** B. Musci, <https://orcid.org/0000-0002-2693-0543>; A. Cheminet, <https://orcid.org/0000-0002-0702-9194>; C. Cuvier, <https://orcid.org/0000-0001-6108-6942>; P. Braganca, <https://orcid.org/0009-0005-5290-1913>; D. Geneste, <https://orcid.org/0009-0007-7341-2590>; JM. Foucaut, <https://orcid.org/0000-0003-0800-8608>; B. Dubrulle, <https://orcid.org/0000-0002-3644-723X>

## REFERENCES

- ASHURST, W. T., KERSTEIN, A. R., KERR, R. M. & GIBSON, C. H. 1987 Alignment of vorticity and scalar gradient with strain rate in simulated Navier-Stokes turbulence. *Phys. Fluids* **30** (8), Aug. 1987), 2343–2353.
- BETCHOV, R. 1956 An inequality concerning the production of vorticity in isotropic turbulence. *Journal of Fluid Mechanics* **1** (5), 497–504.
- BUARIA, DHAWAL, BODENSCHATZ, EBERHARD & PUMIR, ALAIN 2020 Vortex stretching and enstrophy production in high Reynolds number turbulence. *Physical Review Fluids* **5** (10), 1–17, arXiv: 2006.01312.
- BUARIA, DHAWAL & PUMIR, ALAIN 2021 Nonlocal amplification of intense vorticity in turbulent flows. *Physical Review Research* **3** (4), 1–5, arXiv: 2106.14370.
- BUARIA, DHAWAL & PUMIR, ALAIN 2022 Vorticity-Strain Rate Dynamics and the Smallest Scales of Turbulence. *Physical Review Letters* **128** (9), 94501, arXiv: 2202.01364.
- BUARIA, DHAWAL, PUMIR, ALAIN, BODENSCHATZ, EBERHARD & YEUNG, P. K. 2019 Extreme velocity gradients in turbulent flows. *New Journal of Physics* **21** (4), arXiv: 1901.09989.
- BUXTON, O. R.H. & GANAPATHISUBRAMANI, B. 2010 Amplification of enstrophy in the far field of an axisymmetric turbulent jet. *Journal of Fluid Mechanics* **651**, 483–502.
- CANTWELL, BRIAN J 1992 Exact solution of a restricted Euler equation for the velocity gradient tensor. *Physics of Fluids A: Fluid Dynamics* **4**, 782–793.
- CARBONE, M & BRAGG, A D 2020 Is vortex stretching the main cause of the turbulent energy cascade? *Journal of Fluid Mechanics* **883**, 1–13, arXiv: 1906.07144.
- CHEMINET, ADAM, GENESTE, DAMIEN, BARLET, ANTOINE, OSTOVAN, YASAR, CHAABO, TAREK, VALORI, VALENTINA, DEBUE, PAUL, CUVIER, CHRISTOPHE, DAVIAUD, FRANÇOIS, FOUCAUT, JEAN MARC, LAVAL, JEAN PHILIPPE, PADILLA, VINCENT, WIERTEL-GASQUET, CÉCILE & DUBRULLE, BÉRENGÈRE 2022 Eulerian vs Lagrangian Irreversibility in an Experimental Turbulent Swirling Flow. *Physical Review Letters* **129** (12), 124501.
- CHEMINET, ADAM, OSTOVAN, YASAR, VALORI, VALENTINA, CUVIER, CHRISTOPHE, DAVIAUD, FRANÇOIS, DEBUE, PAUL, DUBRULLE, BÉRENGÈRE, FOUCAUT, JEAN MARC & LAVAL, JEAN PHILIPPE 2021 Optimization of regularized B-spline smoothing for turbulent Lagrangian trajectories. *Experimental Thermal and Fluid Science* **127** (June 2020).
- CHEVILLARD, L. & MENEVEAU, C. 2006 Lagrangian dynamics and statistical geometric structure of turbulence. *Physical Review Letters* **97** (17), 1–4, arXiv: 0606267.
- CHEVILLARD, L., MENEVEAU, C., BIFERALE, L. & TOSCHI, F. 2008 Modeling the pressure Hessian and viscous Laplacian in turbulence: Comparisons with direct numerical simulation and implications on velocity gradient dynamics. *Physics of Fluids* **20** (10).
- CHONG, M. S., PERRY, A. E. & CANTWELL, B. J. 1990 A general classification of three-dimensional flow fields. *Physics of Fluids A* **2** (5), 765–777.
- CORTET, P. P., CHIFFAUDEL, A., DAVIAUD, F. & DUBRULLE, B. 2010 Experimental evidence of a phase transition in a closed turbulent flow. *Physical Review Letters* **105** (21), 214501.
- DANISH, MOHAMMAD & MENEVEAU, CHARLES 2018 Multiscale analysis of the invariants of the velocity gradient tensor in isotropic turbulence. *Physical Review Fluids* **3** (4), 1–22.
- DEBUE, PAUL, KUZAY, DENIS, SAW, EWE WEI, DAVIAUD, FRANÇOIS, DUBRULLE, BÉRENGÈRE, CANET, LÉONIE, ROSSETTO, VINCENT & WSCHEBOR, NICOLÁS 2018a Experimental test of the crossover between the inertial and the dissipative range in a turbulent swirling flow. *Physical Review Fluids* **3** (2), 024602.
- DEBUE, P., SHUKLA, V., KUZAY, D., FARANDA, D., SAW, E. W., DAVIAUD, F. & DUBRULLE, B. 2018b Dissipation, intermittency, and singularities in incompressible turbulent flows. *Physical Review E* **97** (5), 053101.

- DEBUE, P, VALORI, V, CUVIER, C, DAVIAUD, F, FOUCAUT, J M, LAVAL, J P, WIERTEL, C, PADILLA, V & DUBRULLE, B 2021 Three-dimensional analysis of precursors to non-viscous dissipation in an experimental turbulent flow. *Journal of Fluid Mechanics* **914**, 1–20.
- DONZIS, D A, YEUNG, P K & SREENIVASAN, K R 2008 Dissipation and enstrophy in isotropic turbulence: Resolution effects and scaling in direct numerical simulations. *Physics of Fluids* **20** (4).
- DUBRULLE, BÉRENGÈRE 2019 Beyond Kolmogorov cascades. *Journal of Fluid Mechanics* **867**, P1.
- DUBRULLE, BÉRENGÈRE, DAVIAUD, FRANÇOIS, FARANDA, DAVIDE, MARIÉ, LOUIS & SAINT-MICHEL, BRICE 2022 How many modes are needed to predict climate bifurcations? Lessons from an experiment. *Nonlinear Processes in Geophysics* **29** (1), 17–35.
- DUCHON, JEAN & ROBERT, RAOUL 2000 Inertial energy dissipation for weak solutions of incompressible Euler and Navier-Stokes equations. *Nonlinearity* **13** (1), 249–255.
- ELSINGA, G. E. & MARUSIC, I. 2010 Universal aspects of small-scale motions in turbulence. *Journal of Fluid Mechanics* **662**, 514–539.
- GENESTE, DAMIEN, FALLER, HUGUES, NGUYEN, FLORIAN, SHUKLA, VISHWANATH, LAVAL, JEAN PHILIPPE, DAVIAUD, FRANCOIS, SAW, EWE WEI & DUBRULLE, BÉRENGÈRE 2019 About Universality and Thermodynamics of Turbulence. *Entropy 2019, Vol. 21, Page 326* **21** (3), 326.
- GESEMANN, SEBASTIAN, HUH, FLORIAN, SCHANZ, DANIEL & SCHRÖDER, ANDREAS 2016 From noisy particle tracks to velocity, acceleration and pressure fields using B-splines and penalties. *18Th International Symposium on Applications of Laser and Imaging Techniques To Fluid Mechanics* (January).
- GULITSKI, G., KholmYANSKY, M., KINZELBACH, W., LÜTHI, B., TSINOBER, A. & YORISH, S. 2007 Velocity and temperature derivatives in high-Reynolds-number turbulent flows in the atmospheric surface layer. Part 1. Facilities, methods and some general results. *Journal of Fluid Mechanics* **589**, 57–81.
- HAMLINGTON, PETER E, SCHUMACHER, JÖG & DAHM, WERNER J A 2008 Direct assessment of vorticity alignment with local and nonlocal strain rates in turbulent flows. *Physics of Fluids* **20** (11), 1–5, arXiv: 0810.3439.
- ISHIHARA, TAKASHI, GOTOH, TOSHIYUKI & KANEDA, YUKIO 2009 Study of high-reynolds number isotropic turbulence by direct numerical simulation. *Annual Review of Fluid Mechanics* **41**, 165–180.
- JIMÉNEZ, JAVIER 1992 Kinematic alignment effects in turbulent flows. *Physics of Fluids A* **4** (4), 652–654.
- JIMENEZ, JAVIER, WRAY, ALAN A, SAFFMAN, PHILIP G & ROGALLO, ROBERT S 1993 The structure of intense vorticity in isotropic turbulence. *Journal of Fluid Mechanics* **255**, 65–90.
- JOHNSON, PERRY L. 2020 Energy Transfer from Large to Small Scales in Turbulence by Multiscale Nonlinear Strain and Vorticity Interactions. *Physical Review Letters* **124** (10), 104501, arXiv: 1912.00293.
- JOHNSON, PERRY L. 2021 On the role of vorticity stretching and strain self-amplification in the turbulence energy cascade. *Journal of Fluid Mechanics* **922**, 1–37, arXiv: 2102.06844.
- JOHNSON, PERRY L. & WILCZEK, MICHAEL 2024 Multiscale Velocity Gradients in Turbulence. *Annual Review of Fluid Mechanics* **56**, 463–490.
- KUZZAY, DENIS, FARANDA, DAVIDE & DUBRULLE, BÉRENGÈRE 2015 Global vs local energy dissipation: The energy cycle of the turbulent von Kármán flow. *Physics of Fluids* **27** (7), arXiv: 1507.00277.
- ONSAGER, L. 1949 Statistical hydrodynamics. *Il Nuovo Cimento Series* **9** **6** (2 Supplement), 279–287.
- RAVELET, FLORENT, MARIÉ, LOUIS, CHIFFAUDEL, ARNAUD & DAVIAUD, FRANÇOIS 2004 Multistability and memory effect in a highly turbulent flow: Experimental evidence for a global bifurcation. *Physical Review Letters* **93** (16), 2–5.
- ROSALES, CARLOS & MENEVEAU, CHARLES 2006 A minimal multiscale Lagrangian map approach to synthesize non-Gaussian turbulent vector fields. *Physics of Fluids* **18** (7).
- SCHANZ, DANIEL, GESEMANN, SEBASTIAN & SCHRÖDER, ANDREAS 2016 Shake-The-Box: Lagrangian particle tracking at high particle image densities. *Experiments in Fluids* **57** (5), 1–27.
- SMAGORINSKY, J. 1963 General Circulation Experiments with the Primitive Equations I. The Basic Experiment. *Monthly Weather Review* **12** (306), 731–732.
- SUMAN, SAWAN & GIRIMAJI, SHARATH S. 2010 Velocity gradient invariants and local flow-field topology in compressible turbulence. *Journal of Turbulence* **11**, 1–24.
- TSINOBER, A. 1998 Is concentrated vorticity that important? *European Journal of Mechanics, B/Fluids* **17** (4), 421–449.
- TSINOBER, ARKADY 2009 *An informal conceptual introduction to turbulence*, 2nd edn., , vol. 92. Springer, Dordrecht.
- TSINOBER, A. & KIT, E. 1992 Experimental investigation of the field of velocity gradients in turbulent flows. *Journal of Fluid Mechanics* **242** (24), 169–192.

- VELA-MARTÍN, ALBERTO & JIMÉNEZ, JAVIER 2021 Entropy, irreversibility and cascades in the inertial range of isotropic turbulence. *Journal of Fluid Mechanics* **915**, 1–33, arXiv: 2005.03602.
- VIEILLEFOSSE, P. 1982 Local Interaction Between Vorticity and Shear in a Perfect Incompressible Fluid. *Journal de physique Paris* **43** (6), 837–842.
- VIEILLEFOSSE, P. 1984 Internal motion of a small element of fluid in an inviscid flow. *Physica A: Statistical Mechanics and its Applications* **125** (1), 150–162.
- VINCENT, A. & MENEGUZZI, M. 1994 The dynamics of vorticity tubes in homogeneous turbulence. *Journal of Fluid Mechanics* **258** (5-6), 245–254.
- XU, HAITAO, PUMIR, ALAIN & BODENSCHATZ, EBERHARD 2011 The pirouette effect in turbulent flows. *Nature Physics* **7** (9), 709–712.
- YAO, JIE & HUSSAIN, FAZLE 2020 On singularity formation via viscous vortexA reconnection. *Journal of Fluid Mechanics* **888**, 1–12.
- YAO, JIE & HUSSAIN, FAZLE 2021 Vortex Reconnection and Turbulence Cascade. *Annual Review of Fluid Mechanics* **54**, 317–347.
- ZHOU, BO & FRANK, JONATHAN H. 2021 Experimental study of vorticity-strain interactions in turbulent premixed counterflow flames. *Proceedings of the Combustion Institute* **38** (2), 2909–2916.